

Mechanisms for High Selectivity in Hydrodeoxygenation of 5-Hydroxymethylfurfural over PtCo Nanocrystals

Jing Luo, Hongseok Yun, Alexander V. Mironenko, Konstantinos A. Goulas, Jennifer D. Lee, Matteo Monai, Cong Wang, Vassili Vorotnikov, Christopher B. Murray, Dionisios G. Vlachos, Paolo Fornasiero, and Raymond J. Gorte

ACS Catal., **Just Accepted Manuscript** • Publication Date (Web): 20 May 2016

Downloaded from <http://pubs.acs.org> on May 20, 2016

Just Accepted

“Just Accepted” manuscripts have been peer-reviewed and accepted for publication. They are posted online prior to technical editing, formatting for publication and author proofing. The American Chemical Society provides “Just Accepted” as a free service to the research community to expedite the dissemination of scientific material as soon as possible after acceptance. “Just Accepted” manuscripts appear in full in PDF format accompanied by an HTML abstract. “Just Accepted” manuscripts have been fully peer reviewed, but should not be considered the official version of record. They are accessible to all readers and citable by the Digital Object Identifier (DOI®). “Just Accepted” is an optional service offered to authors. Therefore, the “Just Accepted” Web site may not include all articles that will be published in the journal. After a manuscript is technically edited and formatted, it will be removed from the “Just Accepted” Web site and published as an ASAP article. Note that technical editing may introduce minor changes to the manuscript text and/or graphics which could affect content, and all legal disclaimers and ethical guidelines that apply to the journal pertain. ACS cannot be held responsible for errors or consequences arising from the use of information contained in these “Just Accepted” manuscripts.



Mechanisms for High Selectivity in Hydrodeoxygenation of 5-Hydroxymethylfurfural over PtCo Nanocrystals

Jing Luo^{a,†}, Hongseok Yun^{b,†}, Alexander V. Mironenko^{c,†}, Konstantinos Goulas^c, Jennifer D. Lee^b, Matteo Monai^d, Cong Wang^a, Vassili Vorotnikov^c, Christopher B. Murray^b, Dionisios G. Vlachos^c, Paolo Fornasiero^d and Raymond J. Gorte^{a,*}

^aDepartment of Chemical & Biomolecular Engineering, University of Pennsylvania
Philadelphia, PA 19104, United States

^bDepartment of Chemistry, University of Pennsylvania
Philadelphia, PA 19104, United States

^cDepartment of Chemical & Biomolecular Engineering, University of Delaware
Newark, DE 19716, United States

^dDepartment of Chemical and Pharmaceutical Sciences, University of Trieste
Trieste, 34127, Italy

Abstract

Carbon-supported, Pt and PtCo nanocrystals (NCs) with controlled size and composition were synthesized and examined for hydrodeoxygenation (HDO) of 5-hydroxymethylfurfural (HMF). Experiments in a continuous flow reactor with 1-propanol solvent, at 120 to 160°C and 33 bar H₂, demonstrated that reaction is sequential on both Pt and PtCo alloys, with 2,5-dimethylfuran (DMF) formed as an intermediate product. However, the reaction of DMF is greatly suppressed on the alloys, such that a Pt₃Co₂ catalyst achieved DMF yields as high as 98%. XRD and XAS data indicate that the Pt₃Co₂ catalyst consists of a Pt-rich core and a Co oxide surface monolayer whose structure differs substantially from that of bulk Co oxide. Density functional theory (DFT) calculations reveal that the oxide monolayer interacts weakly with the furan ring to prevent side reactions, including over-hydrogenation and ring opening, while providing sites for effective HDO to the desired product, DMF. We demonstrate that control over metal nanoparticle size and composition, along with operating conditions, is crucial to achieving good performance and stability. Implications of this mechanism for other reactions and catalysts are discussed.

Keywords: 5-hydroxymethylfurfural, hydrodeoxygenation, 2,5-dimethyl furan, PtCo nanocrystal, bimetallic catalyst

† These authors contribute equally.

* Corresponding Author: Raymond J. Gorte

Email: gorte@seas.upenn.edu

INTRODUCTION

5-Hydroxymethylfurfural (HMF) is a key platform chemical in biomass conversion.^{1,2} It is readily obtained by the acid-catalyzed dehydration of C-6 sugars (e.g. fructose, but its high degree of functionality precludes its direct use as a fuel.³⁻⁵ One promising approach to stabilize HMF is the selective hydrodeoxygenation to form 2,5-dimethylfuran (DMF). A relatively small amount of hydrogen is consumed in the formation of DMF and DMF can be used directly as fuel additive due to its high energy density and an octane rating of 119.⁶ DMF can also be converted to p-xylene via a Diels-Alder reaction with ethylene.⁷

The reaction of HMF to DMF has been studied extensively over various metal and metal-alloy catalysts⁸⁻¹⁰ but selectivity to DMF over ring-opened (e.g. 2-hexanone, 2,5-hexanedione) and ring-hydrogenated (e.g. 2,5-dimethyl tetrahydrofuran) products is often poor. Understanding what is required for a good catalyst is made more difficult by the large variances in yields that have been reported by different groups for materials of similar composition.^{11,12} Some of these variances appear to be due the sensitivity of results to the type of reactor that is used in the rate measurements.¹³ Even so, bimetallic catalysts appear to be more selective than their pure-metal analogs.¹⁴⁻¹⁶ For example, Schüth and co-workers¹⁷ reported DMF yields as high as 98% on Pt-Co nanoparticles which were encapsulated in hollow carbon spheres.

Some of us have recently reported that the reaction of HMF to DMF is sequential on Pt and many other metals¹⁸, with HMF reacting selectively to DMF, but DMF then going on to form secondary products over the same catalysts. Based on these mechanistic considerations, the yield of DMF is determined by the relative rates of DMF formation and DMF consumption and the most selective catalysts should show low activity for reaction of DMF. An implication of this picture is that selective catalysts cannot consist of a mixture of selective and nonselective components, since even a relatively small fraction of nonselective material could convert DMF to other products. For the case in which two metals are nonselective (e.g. Pt and Co)¹⁸ but their alloy is selective, this means that the composition of the metal particles must be uniform.

The synthesis of highly uniform Pt and PtCo nanocrystals (NCs) have demonstrated via solvothermal methods.^{19,20} The solvothermal method can readily control the size, morphology, and composition of NCs and these parameters are strongly correlated to their catalytic properties.^{20,21} For example, Huang *et al.* reported that small amounts of molybdenum doping into Pt₃Ni NCs can enhance its specific activity for the oxygen reduction reaction by 81 fold

1
2
3 compared with the activity of a commercial Pt/C catalyst.²² Therefore, this synthetic approach
4 enables us to prepare and test catalysts whose properties are well controlled, allowing us to
5 understand the effect of various parameters on catalytic activities.
6
7

8
9 Here, we report the HDO of HMF into DMF catalyzed by Pt, Pt₃Co, and Pt₃Co₂ NCs
10 using a continuous flow reactor. DMF yields as high as 98% were achieved with Pt₃Co₂ alloys
11 because this alloy shows a very low reactivity towards DMF. Furthermore, the bimetallic
12 catalysts synthesized using the solvothermal method are stable and superior to alloy catalysts
13 prepared by traditional wet impregnation. Characterization of the Pt-Co NCs reveals they have a
14 special structure consisting of a monolayer of surface oxide on a metallic core. Calculations
15 using Density functional theory (DFT) rationalize the stability of this structure and indicate that
16 the oxide prevents side reactions while providing catalytic sites for effective conversion of HMF
17 to DMF. Computations reveal a radical-mediated reaction mechanism, which some of us have
18 found to be critical for selective HDO on oxides.²³ Structural characterization and DFT
19 calculations confirm that controlling the bimetallic composition is essential for preparing a good
20 catalyst.
21
22
23
24
25
26
27
28
29
30
31

32 **METHODS**

33 **Catalyst synthesis and characterization**

34
35 Nearly monodisperse Pt, Pt₃Co, and Pt₃Co₂ NCs were synthesized by using or modifying
36 the reported methods.^{19,20} (See Supporting Information Section S1 for further details) To prepare
37 Pt NCs, platinum (II) acetylacetonate (acac) dissolved in 20 mL of benzyl ether was decomposed
38 at 300 °C in the presence of oleic acid, oleylamine, and trioctylphosphine under nitrogen. For
39 platinum cobalt bimetallic NC synthesis, the hot injection technique of dicobalt octacarbonyl
40 (Co₂(CO)₈) is employed. In the synthesis of Pt₃Co, the reaction mixture of Pt(acac)₂, 1-
41 adamantane carboxylic acid, 1,2-hexadecanediol (HDD), and hexadecylamine were heated under
42 nitrogen and Co₂(CO)₈ was injected into the reaction mixture at 170 °C. The reaction mixture is
43 heated up to 230 °C. After 40 mins, the reaction mixture was cooled down to room temperature.
44 In this case, HDD was used to reduce Pt, which is called “polyol process”²⁴. On the other hand,
45 for the synthesis of Pt₃Co₂, hexadecylamine was replaced by oleylamine and HDD was not
46 added. After the injection of Co₂(CO)₈ at 170 °C, the reaction vessel was heated to 300 °C and
47 kept for 30 mins. As oleylamine is a relatively milder reducing agent than HDD,²⁵ this reaction
48
49
50
51
52
53
54
55
56
57
58
59
60

1
2
3
4
5
6
7
8
9
10
11
12
13
14
15
16
17
18
19
20
21
22
23
24
25
26
27
28
29
30
31
32
33
34
35
36
37
38
39
40
41
42
43
44
45
46
47
48
49
50
51
52
53
54
55
56
57
58
59
60

resulted in relatively cobalt rich NCs compared to the reaction done by the polyol process. From the Transmission Electron Microscope (TEM) images of NCs in Figure 1, the average diameters of NCs were 2.4 nm, 3.2 nm, and 3.7 nm with less than 8% of size distribution for Pt, Pt₃Co, and Pt₃Co₂ NCs, respectively. A superlattice structure for each composition of NCs was observed, indicating the high monodispersity of these NCs. Wide angle x-ray scattering data show that all the NCs possess face-centered cubic (fcc) crystal structure as displayed in Figure 1d. The compositions of NCs were confirmed by Inductively Coupled Plasma Optical Emission Spectrometry (ICP-OES).

The NCs are dispersed into carbon support to prepare 10 weight % of metals on carbon. (Supplementary information for further details about the preparation procedure) As the colloidal NCs are covered by organic ligands, such as oleic acid and oleylamine, for colloidal stability, the catalytic reactions are inhibited due to the limited access of reactants to the binding sites on the NC surface. Therefore, the surface ligands should be removed to maximize their available surface area. For this purpose, the catalysts were gone through the two steps of surface treatment. First, the 300 mg of 10 wt % metal/C catalysts were exposed to O₂ plasma for 15 mins. After the plasma treatment, the NC surface was further cleaned by rapid thermal annealing (RTA).²⁶ Figure S1 shows TEM images of as-deposited and surface ligand removed NCs on carbon support. After the plasma and thermal treatment, no significant change in size and morphology is observed in all the cases of NCs, which proves the reliability of our surface treatment technique. Also, from wide angle x-ray scattering study (Figure S2), it is confirmed that the phase of Pt₃Co and Pt₃Co₂ is not transformed from disordered fcc to ordered fct structure. Therefore, we can exclude the potential effects of crystal structure ordering on the catalytic activity and attribute any difference to the compositional effect.²⁷

The metal dispersions were determined volumetrically using CO adsorption uptakes at room temperature on Al₂O₃ supported catalysts. CO chemisorption experiments were performed on alumina supported NCs in order to avoid sorption problems related to active carbon supports.²⁸ 0.1 g Catalyst was loaded into a sample cell, evacuated at 400°C and reduced for 30 minutes at 250°C or 400°C in 200 Torr of H₂. Finally, the sample was evacuated and cooled to room temperature. CO uptakes were then determined by adding small pulses of CO until a rise in the pressure of the sample cell was detected. In determining the NCs dispersion, we assumed an adsorption stoichiometry of one CO molecule per surface Pt.²⁹ Chemisorption of CO on Co was

1
2
3 not included in the calculation of the dispersion because control experiments on Co/Al₂O₃
4 catalysts prepared by impregnation method reduced at 400°C did not show any CO adsorption.

7 **Liquid-phase HDO with H₂ in a flow reactor**

8
9 The three-phase reactions were carried out in a continuous flow reactor that has been
10 described in detail elsewhere.^{13,18} The reactor was a stainless-steel tube, 20-cm long, with a 4.6-
11 mm ID. In most cases, 0.05 g of catalyst was packed into the middle portion of the tube and held
12 in place by glass wool; however, conversions and selectivities were dependent only on reactor
13 space time, independent of reactor catalyst loading. An inert glass tube was placed in the
14 stainless-steel tube, downstream from the catalyst, in order to reduce the empty volume of the
15 reactor and to prevent the catalyst bed from being pushed out of the heated zone by the reactant
16 flow. The liquid feed, either a mixture of 1.0 g HMF (99%, Sigma-Aldrich) or 0.76 g DMF (99%,
17 Sigma-Aldrich) in 100 mL of 1-propanol (Fisher Scientific), was introduced into the reactor by
18 an HPLC pump (Series I+, Scientific Systems Inc.), which was also used to measure the total
19 pressure in the reactor. (The reaction of DMF was performed with 0.76 g of DMF in 100 ml of 1-
20 propanol to maintain the same molar concentration as that used in the HMF rate measurements.)
21 The H₂ (UHP grade, Airgas) flow to the reactor was controlled by varying the pressure drop
22 across 8 feet of 0.002-inch ID capillary tubing (Valco Instruments, Inc.). A bubble meter at the
23 reactor exit was used periodically to check the H₂ flow rates. The liquid flow rates could be
24 varied from 0.02 to 0.2 ml/min, while the H₂ flow rates were 2 to 20 mL/min (STP). In order to
25 vary the space velocity in the reactor at fixed experimental conditions, the ratio of liquid and gas
26 flow rates was kept constant. The pressure within the reactor was controlled by a back-pressure
27 regulator (KPB series, Swagelok) placed at the reactor exit.

28
29
30
31
32
33
34
35
36
37
38
39
40
41
42
43
44
45
46
47
48
49
50
51
52
53
54
55
56
57
58
59
60
Prior to rate measurements, the catalyst was pretreated at 250°C in 1 bar of flowing H₂ for
30 min. Because the products left the reactor at room temperature, product analysis was carried
out using a syringe to inject the liquid effluent into a GC-MS (QP-5000, Shimadzu), equipped
with a capillary column (HP-Innowax, Agilent Technologies). The gas-phase products were also
examined but, under the conditions of these experiments, were found to consist of only H₂ and
solvent vapor. Product selectivities were quantified using standard solutions with known
concentrations of HMF, DMF, DMTHF, 2-hexanone, 2-hexanol, and 2,5-hexandione (all
purchased from Sigma Aldrich). For quantification of other furan-based, intermediate products,
the GC sensitivity was assumed to be the same as that for HMF. For open-ring, ether products,

1
2
3 the GC sensitivity was assumed to be the same as 2-hexanone or 2,5-hexandione. The carbon
4 balance from GC analysis was always better than 95%.
5
6

7 The typical time for an experiment was 4 h. For each sample injection, the GC analysis
8 required 30 min. Most of the data reported here were chosen from the second or third
9 measurement (40 to 60 min after starting the reaction). For the conditions of this study, no
10 reaction was observed in the absence of a catalyst in the flow reactor.
11
12
13

14 **X-ray Absorption Measurements**

15 X-ray absorption measurements were performed at the beamline 5BM-D at the Advanced
16 Photon Source, Argonne National Laboratory. Catalyst samples were diluted with boron nitride
17 and pressed into pellets in a six-well sample holder. The catalysts were reduced at 250 °C (pre-
18 treatment temperature) and 400 °C (higher than the pretreatment temperature) for 1 h (ramp rate
19 5 °C min⁻¹) under atmospheric pressure in a 40 ml min⁻¹ hydrogen flow prior to measurement at
20 ambient temperature under hydrogen. Data processing was done using the program Athena of the
21 Demeter suite. Fitting of the EXAFS oscillations was done using the Artemis program of the
22 same suite. For the Pt L3 edge, oscillations were fitted using the Fourier transform (FT) from
23 wavenumbers $k = 3 \text{ \AA}^{-1}$ to $k = 12 \text{ \AA}^{-1}$ and $R = 1.6 \text{ \AA}$ to 3.3 \AA while for the Co K edge,
24 oscillations were fitted using a FT from wavenumbers $k = 3 \text{ \AA}^{-1}$ to $k = 12 \text{ \AA}^{-1}$, and $R = 1.4 \text{ \AA}$ to R
25 $= 3.2 \text{ \AA}$. Amplitude reduction factors were calculated using the EXAFS spectrum of the Pt or Co
26 foils and assuming a coordination number (CN) equal to 12. A single Debye-Waller factor was
27 used for all scattering paths.
28
29
30
31
32
33
34
35
36
37
38

39 **Density functional theory (DFT) calculations**

40 Spin-polarized density functional theory calculations have been carried out under the
41 generalized gradient approximation using VASP software³⁰⁻³². Kohn-Sham eigenstates have
42 been expanded in a plane wave basis set with a kinetic energy cutoff of 400 eV. Sampling of the
43 first Brillouin zone has been carried out according to the Monkhorst-Pack³³ 3x3x1 k-point mesh.
44 The initial magnetic moment of Co atoms has been set to 2.0 Bohr-magnetons. Exchange,
45 correlation, and dispersion effects have been approximated with a PBE-D3^{34,35} functional.
46 Threshold value for maximum atomic forces has been set to 0.05 eV/Å. Transition states have
47 been identified via a climbing-image nudged elastic band (CINEB) and/or a dimer³⁶⁻³⁹ method
48 with the forces' tolerance set to 0.1 eV/Å. A honeycomb Co₃O₂ on a Pt-rich metallic core has
49 been modeled as a Co₃O₂/Pt(111) surface using a (4x4) supercell with a honeycomb Co₃O₂
50
51
52
53
54
55
56
57
58
59
60

1
2
3 structure placed on top of three Pt layers (bottom two were fixed). We used a finite difference
4 method to calculate selected vibrational frequencies. Throughout the paper, DFT energies in a
5 vacuum are reported, unless stated otherwise.
6
7

8 9 10 **RESULTS**

11 **HDO Studies**

12
13 Previous studies on carbon-supported Pt and Co catalysts have shown that
14 hydrodeoxygenation of HMF to DMF is a series reaction¹⁸, proceeding as indicated in Scheme 1.
15 The HMF (A) first reacts to a group of partially hydrogenated intermediate compounds (B),
16 including 2-propoxymethyl-5-furanmethanol (ether-furfuryl alcohol, or EFA), 2-propoxymethyl-
17 5-methylfuran (ether-methyl furan, or EMF), 5-methyl furfural (MF), 2-hydroxymethyl-5-
18 methyl furan (HMMF), 2,5-bis(hydroxymethyl)furan (BHMF), and 2,5-bis(propoxymethyl)furan
19 (BEF). These intermediate compounds can all be converted to DMF (C), which in turn reacts to
20 over-hydrogenated products (D), dimethyl tetrahydrofuran (DMTHF), 2-hexanone, 2-hexanol,
21 2,5-hexanedione, and their etherification derivatives, 1-propoxy-1-methyl-pentane (2-
22 propoxyhexane) and 1,4-dipropoxy-1,4-dimethyl-butane (2,5-dipropoxyhexane).
23
24
25
26
27
28
29
30

31 Figure 2a, which is a plot of the conversion and product yield as a function of space time
32 on the 10-wt% Pt/C catalyst prepared from Pt NCs, shows that Scheme 1 also applies to reaction
33 of HMF in this case. These experiments were carried out at 120°C, a significantly lower
34 temperature than that used in a previous study with Pt catalysts prepared by infiltration of metal
35 salts, because the NCs catalysts were much more active. Even for the shortest space time and at
36 this low temperature, the HMF conversion was greater than 65%. Initially, partially
37 hydrogenated products, B, were formed in the highest yields, but these declined steadily with
38 increasing space time. DMF yield initially increased, then decreased, providing strong evidence
39 that DMF is an intermediate product in a series reaction. The maximum yield was approximately
40 41%. Over-hydrogenated compounds, D, only formed at higher space times, indicating that they
41 are not primary products. The fact that their formation follows the consumption of DMF strongly
42 suggests they are formed from DMF. A detailed analysis of the partially hydrogenated (B) and
43 over-hydrogenated (D) compounds is given in the Supplemental Information, Table S1 and
44 Figure S3a. The HDO of HMF over Co/C has been reported in a previous study¹⁸. The products
45 formed as a function of space time were similar to that formed over Pt catalysts. Co itself is not
46 selective to DMF, due to the formation of the over-hydrogenated product, 2,5-hexanedione, at
47
48
49
50
51
52
53
54
55
56
57
58
59
60

1
2
3 high space times. Similar experiments were performed on the 10 wt-% Pt-Co, NCs catalysts, with
4 Pt:Co ratios of 3:1 and 3:2. Data at 120°C and 33 bar are shown in Figure 2b and 2c. For a given
5 space time, the HMF conversions over the Pt₃Co in Figure 2b were slightly lower than that
6 obtained on the pure Pt NCs; but the initial products were the same partially hydrogenated
7 compounds, B (see Table S1), with these again being converted to DMF at a similar rate.
8 However, on the Pt₃Co catalyst, the DMF yield continued to increase, to a value of 75%; and
9 only relatively small quantities of over-hydrogenated compounds, D, were formed at the largest
10 space times. The activity of the Pt₃Co₂ catalyst was noticeably lower than that of the other two
11 samples, and 100% conversion of HMF was achieved only at the highest space time. Because of
12 the lower activity, the DMF yield was still increasing at the highest space time and the
13 production of D-group compounds was negligible.

14
15 Due to the lower rates on the Pt-Co catalysts, additional reaction measurements were
16 performed at 160°C and 33 bar in order to determine the evolution of products, with results shown
17 in Figure 3. As shown in Figure 3a, the HMF conversion was nearly 90% on the Pt₃Co sample,
18 even at the lowest space time. The B-products again decline steadily with time but DMF yield
19 went through a maximum of about 75% at this temperature, with over-hydrogenated products
20 being produced from the DMF. However, results for the Pt₃Co₂ sample in Figure 3b show the
21 DMF yields continuing to increase, up to 98%.

22
23 The Pt₃Co₂ sample was also very stable compared to the Pt catalyst. Figure 4 shows the
24 HMF conversion and DMF yield for the two catalysts as a function of time at 160°C and a space
25 of 1.0 g·min/mL. The Pt-Co catalysts has no observable deactivation or change in selectivity for
26 a period of at least 14 h. By contrast, the Pt/C deactivated rapidly under these same conditions. It
27 should be noted that Pt/C catalyst was highly active under these conditions, so that the low initial
28 yield is due to the “over-reaction” of DMF to over-hydrogenated (D) compounds. The increasing
29 yield with short times results from the lower catalyst activity. In addition to the stability against
30 coking, the alloy catalyst is also more thermally stable.⁴⁰ Figure S1 has shows TEM images for
31 Pt and PtCo catalysts after 5 hours reaction at 160°C. The average size of Pt NCs increased and
32 some aggregates formed, while the size and shape of Pt₃Co₂ NCs remained unchanged. In Figure
33 S4 and Table S2, statistical particle size analysis is presented. Pt NCs underwent morphological
34 changes, with the average particle size increasing from 2.4 nm to 3.5 nm and a significant size
35 distribution change from 7.3 % to 19 %. By contrast, Pt₃Co₂ NCs showed almost no
36
37
38
39
40
41
42
43
44
45
46
47
48
49
50
51
52
53
54
55
56
57
58
59
60

morphological change. The average size of the particles were unaffected and the size distribution increased only slightly from 7.3 % to 10 %.

The results in Figure 2 and Figure 3 indicate that Co alloying with Pt has a modest effect on HDO rates for HMF but strongly suppresses reactions of DMF. To investigate this in more detail, we examined the reaction of DMF on the same three catalysts, with conversions and product distributions shown in Figure 5. The reactions were again carried out at 33 bar and either 120°C (for Pt) or 160°C (for the Pt-Co alloys), using 1-propanol solutions with the same DMF molarity as that used in the HMF experiments. Because water is formed in the reaction of HMF, these experiments do not perfectly mimic the sequential reaction found in HMF; however, some water was also formed in the DMF reaction measurements by dehydration of the alcohols to form di-propyl ether.

As shown in Figure 5a, DMF is converted rapidly on Pt/C, even at 120°C. The main products are the open-ring ketones and ethers, the products that were also formed at high space times for the reaction of HMF (see Figure S3 in SI). The reaction of DMF on the Pt-Co catalysts was carried out at 160°C because of their lower activities. Even at this higher temperature, DMF conversions on the Pt₃Co sample were lower than that observed on the Pt catalyst, although still significant. The products on the Pt₃Co catalyst were essentially the same as that observed on Pt. However, the conversion of DMF on the Pt₃Co₂ sample at 160°C, shown in Figure 5c, was very low for all space times, reaching a value of only 10% at a space time of 1.0 g·min/mL.

Characterization

In order to understand the role of Co for high HMF-to-DMF selectivity and elucidate the nature of the active site, a combination of microscopic, spectroscopic, and computational tools were employed, as discussed below. First, the compositions of all the NCs samples were checked by Inductively Coupled Plasma/Mass Spectroscopy (ICP-MS) and found to agree with the quoted compositions. Second, the NCs were of uniform size, with an FCC structure, as shown by the TEM and wide angle x-ray scattering results in Figure 1. The uniformity of the particle sizes is demonstrated by the particles packing in regular hexagonal lattices. Wide angle x-ray scattering data (Figure 1d) show that the (220) peak shifts from 67.6° for Pt NCs to 68.2° and 68.4° for Pt₃Co and Pt₃Co₂, indicating the replacement of Pt by Co in the lattice structure. The lattice constants of the NCs, determined from the position of the (220) peak on the x-ray scattering patterns, are 3.92, 3.87, and 3.87 Å for Pt, Pt₃Co, and Pt₃Co₂ NCs, respectively. Using

1
2
3 Vegard's law, the bulk Co fraction in the Pt₃Co and Pt₃Co₂ NCs is estimated to be 13.4 mol.%.
4
5 The fact that the bulk Co fraction is lower than that of the alloy stoichiometry is an initial
6
7 indication of Co segregation.
8

9 The local environments of the Pt and Co atoms were further investigated using X-Ray
10 Absorption Spectroscopy (XAS). The Pt L₃ near-edge spectra of Pt₃Co₂ samples reduced in H₂ at
11 250 and 400°C are shown in Figure 6a, together with the Co K near-edge spectra (Figure 6b). On
12 the Pt edge, the white line and edge positions of the alloy coincide with those of the Pt foil for
13 both reduction temperatures, demonstrating that the Pt is fully reduced in all cases. However, the
14 Extended X-Ray Absorption Fine Structure (EXAFS) on the Pt edge suggests that there is
15 surface segregation of Co in the Pt-Co alloy particles, as the Pt:Co ratio in the Pt coordination
16 sphere (3.1 ± 0.6) is greater than the nominal. Considering the fact that the cobalt precursor was
17 injected at 170 °C in the synthesis, it is reasonable that the Pt-Co alloy NCs had cobalt rich shell,
18 because platinum precursor can be decomposed and nucleated at lower temperature, which
19 possibly formed the core of NCs. The fitting parameters for these spectra are reported in Table
20 S3, columns 3-5. The Co edge EXAFS was not fitted for the sample reduced at 250 °C, as the
21 variables required to completely describe the structure are greater than the number of available
22 independent data points. After reduction at 400°C, the Pt:Co ratio in the Pt coordination sphere is
23 closer to the nominal (2.1 ± 0.4), consistent with at least partial reverse Co segregation to the
24 bulk. A similar reverse segregation phenomenon has been reported previously for PtNi
25 nanoparticles⁴¹.
26
27

28 The X-Ray Absorption Near Edge Spectra (XANES) of the Co K edge, reported in
29 Figure 6b, provides further information on the nature of the alloy NCs. First, the spectra indicate
30 that Co remains partially oxidized, even after reduction at 400°C. Using a linear combination of
31 spectra from CoO and Co standards to fit the results for the alloy catalyst, the average Co
32 oxidation states after reduction at 250°C and 400 °C were 1.2 (60% CoO) and 0.72 (36% CoO),
33 respectively. Surface oxygen is known to induce Co surface segregation in a Pt-Co alloy⁴². In
34 turn, Co forms a surface monolayer oxide with properties distinct from those of the bulk CoO⁴³.
35 As step sites constitute ca. 30% of all surface sites for 3-4 nm nanoparticles⁴⁴ and tend to stay
36 more oxidized than terraces⁴⁵, we assume 30% of surface sites to be composed of Co in the +2
37 oxidation state (see Section S2 for model details). Following an analogous Fe₃O₂/Pt(111)
38
39
40
41
42
43
44
45
46
47
48
49
50
51
52
53
54
55
56
57
58
59
60

structure observed using STM⁴⁶, we consider the rest of the monolayer surface oxide to be Co₃O₂ with a honeycomb structure on a Pt-Co metallic core as a nanoparticle model (Figure 7a).

Table 1 compares XAS/XRD results with geometric estimates of the alloy core/oxide shell spherical nanoparticle model. Overall, the model exhibits excellent agreement with our experimental data, particularly given the approximations invoked. We predict an average Co oxidation state of 1.18, close to the experimental estimated value of 1.20. The low Co oxidation state is consistent with an O:Co atomic ratio of less than 1 on the majority of surface sites. In contrast, a previously observed surface oxide with CoO stoichiometry⁴³ would yield an average oxidation state >1.5, different from the XANES results. The predicted Co content in the bulk alloy (14.4 mol. %) is close to the Vegard's law estimation from XRD (13.4 mol. %). The experimental and geometric Pt-Co and Pt-Pt CNs agree well. The XAS data demonstrate that Pt₃Co₂ NCs, reduced at 250°C, consist of a Pt-rich core with the majority of Co segregated to the surface, forming a CoO_x surface oxide shell. The Co₃O₂ honeycomb monolayer as a dominant surface structure is consistent with XAS results.

Table 1. Average coordination numbers and Co oxidation states for Pt₃Co₂ NCs reduced at 250°C, determined by X-ray absorption spectroscopy and estimated using a spherical core/shell NC model with planes covered by a Co₃O₂ surface oxide monolayer (70%) and step sites covered by CoO (30%). CN stands for “coordination number”.

	XAS/XRD data	Geometric Model
Co oxidation state	1.20 ¹	1.18
Pt-Co CN	2.88 ¹ ± 0.44	2.92
Pt-Pt CN	8.98 ¹ ± 0.57	8.91
Co content in the bulk alloy, %	13.4 ²	14.4

¹XAS data regression; ²XRD analysis (Vegard's law)

Further evidence for Co₃O₂ surface oxide formation comes from CO chemisorption measurements on NCs supported on γ -Al₂O₃, shown in Table S4. After reduction at 250°C, CO adsorption on the Pt₃Co₂ NCs is negligible, consistent with the Pt atoms being covered. After 400°C reduction, CO chemisorption is comparable to what was observed with Pt NCs, due to reverse segregation of Co to the bulk. DFT results indicate that CO interacts weakly with

1
2
3 $\text{Co}_3\text{O}_2/\text{Pt}(111)$ compared to $\text{Pt}(111)$ (ca -0.7 vs. \sim -2 eV binding energy⁴⁶, respectively),
4
5 consistent with the lack of CO adsorption. A similar in magnitude CO binding energy was
6
7 correlated with no CO adsorption in XPS measurements on $\text{Fe}_3\text{O}_2/\text{Pt}(111)$ honeycomb structure⁴⁶.
8
9 The importance of a Co_3O_2 overlayer structure is further supported from DFT calculations,
10
11 discussed next.

12 **Theoretical Insights into the Reaction Mechanism, Catalyst Composition Effects, and** 13 **Catalyst Stability**

14
15 DFT calculations were performed in order to understand the mechanism of the HDO
16
17 reaction, catalyst stability issues, and the differences among the three catalysts (Pt, Pt_3Co , and
18
19 Pt_3Co_2). Regarding the reaction mechanism on the Pt_3Co_2 catalyst, the calculations showed that
20
21 the Co_3O_2 honeycomb monolayer supported on the Pt rich core is capable of catalyzing key
22
23 reaction steps involved in the HMF to DMF conversion. The overall reaction is assumed to
24
25 proceed via the following steps: 1) H_2 dissociation, 2) C=O hydrogenation, and 3) selective HDO
26
27 with concomitant oxygen removal from the surface in the form of water. These steps and their
28
29 activation barriers are reported in Table S5. It is worth noting that we did not consider the EFA
30
31 (see Table S1), one of the B intermediates, in our calculations. The ether intermediates are
32
33 formed by etherification with solvent molecules, and including them would greatly complicate
34
35 the calculations. Moreover, the HDO reaction is not significantly affected by formation of the
36
37 ether products, as shown in a previous study.¹³ The H_2 dissociation step can occur via several
38
39 homolytic and heterolytic dissociation paths (Table S5). The calculations indicate that homolytic
40
41 splitting of a weakly physisorbed H_2 molecule (-0.1 eV binding energy) over a single Co atom is
42
43 most energetically favorable (a 0.7 eV reaction barrier). The final state (0.3 eV more stable than
44
45 gaseous H_2) entails both H atoms bound to Co and Pt atoms in bridging configurations (Figure
46
47 S5, reaction 1, transition state).

48
49 Prior to the C=O hydrogenation step, HMF weakly adsorbs on the surface (-0.8 eV BE);
50
51 hydrogenation of the C=O carbonyl group exhibits a low reaction barrier when it is weakly
52
53 bound to the surface.^{47,48} Specifically, a concerted addition of two H atoms to HMF occurs with
54
55 a 0.8 eV barrier, yielding BHMF. The overall hydrogenation is exothermic (reaction energy of -
56
57 0.6 eV). BHMF can either desorb (0.9 eV desorption energy) or undergo HDO, ultimately
58
59 forming DMF.
60

1
2
3
4
5
6
7
8
9
10
11
12
13
14
15
16
17
18
19
20
21
22
23
24
25
26
27
28
29
30
31
32
33
34
35
36
37
38
39
40
41
42
43
44
45
46
47
48
49
50
51
52
53
54
55
56
57
58
59
60

The subsequent HDO mechanism of BHMF on the Pt-rich particle with Co_3O_2 coating is radical in nature, and is depicted in Figure 8 (Table S5, reactions 7-10). Some of us have found a similar mechanism of furfural HDO to form 2-methyl furan on a Ru/RuO₂ catalyst to be consistent with a range of experimental and computational data.²³ BHMF undergoes C-O bond scission on a honeycomb edge site consisting of two Co atoms (Figure S5), forming a loosely bound radical and an OH group, with a reaction energy of +0.9 eV and a barrier of 1.2 eV. Next, a hydrogen atom transfers from the OH to the radical, yielding HMMF and a chemisorbed oxygen atom. C-O scission occurs similarly on the second hydroxymethyl group (not shown), forming DMF as the final product. The chemisorbed O atom (+1.7 eV binding energy with respect to H₂ and H₂O) reacts rapidly with H₂ (a -1.2 eV exothermic dissociative adsorption with a 0.3 eV barrier) to form co-adsorbed OH and H that subsequently recombine with a 0.2 eV barrier (-0.9 eV reaction energy) to form water. Finally, water desorbs with a +0.4 eV energy to complete the catalytic cycle.

HMF, BHMF, HMMF, and DMF weakly interact with the Co_3O_2 surface (~ -0.8 eV BE, dominated by dispersion forces⁴⁹, as opposed to chemisorption on metal atoms with BE of the order of -2 eV⁵⁰), largely retaining a gaseous-like molecular geometry (Figure S5). The absence of covalent bonding of the ring with the metal surface is key to rationalizing the high selectivity of the catalyst, because opening of the furanic ring and decarbonylation require strong chemisorption of the furan ring in a flat geometry, with partial $\text{sp}^2 \rightarrow \text{sp}^3$ re-hybridization of ring carbon atoms.⁵¹⁻⁵⁶ Lack of covalent bonding between the ring with the Co_3O_2 oxide protects the ring from further side reactions and explains the low reactivity of DMF. The Co_3O_2 surface layer is capable of catalyzing C-O bond hydrogenolysis in HMF that leads to selective production of DMF.

In order to assess the catalyst stability at a H₂-rich environment, we calculated the rate of initiation of Co_3O_2 reduction via vacancy formation, with the details presented in Section S3. Under experimental HDO conditions (160°C, 33 bar H₂), the vacancy formation rate is a factor of 2 lower than under *in situ* XAS conditions (250°C, 1 bar H₂). Furthermore, the vacancy, once formed, is easily reoxidized by BHMF-to-HMMF reactions. This analysis provides a rationalization as to why the Co_3O_2 surface oxide is stable in a reducing reaction environment.

In contrast to the highly selective, oxide-covered Pt₃Co₂ catalyst, Pt carries out facile hydrogenation of the C=O group to BHMF, but dehydroxylates BHMF to form DMF slowly (see

1
2
3 Section S4). Furthermore, the DMF ring interacts strongly with Pt, promoting ring hydrogenation
4 and ring opening with barriers which are lower than that of the dehydroxylation reaction (see
5 Section S4). The computed barriers for HDO of HMF are comparable to the barriers for ring
6 hydrogenation and ring opening of DMF, consistent with the observation that selectivity to DMF
7 is modest.
8
9

10
11
12 Pt₃Co NCs exhibit catalytic properties intermediate between Pt and Pt₃Co₂. Unlike the
13 Pt₃Co₂ NCs, there are not enough Co atoms to completely cover the surface with an oxide
14 monolayer (Table S6); in this catalyst, the surface is predicted to consist of 1/2 Co oxide and
15 ~1/2 Pt atoms. We believe that this significant difference in structure exposes Pt patches on the
16 surface (Figure 7b). The presence of Pt sites at the surface leads to the partial non-selectivity of
17 the Pt₃Co catalyst.
18
19
20
21
22
23

24 DISCUSSION

25
26 The development of better catalysts for HDO of HMF requires an understanding of the
27 reaction mechanism. First, it is important to recognize that the reaction is sequential.^{13,18} The
28 poor selectivity that is observed with many metals is due to the fact that they further catalyze
29 reactions of DMF, the desired product. While it is required that a catalyst has good activity for
30 HDO of HMF, a selective catalyst must also be a poor catalyst for reactions of DMF. The
31 sequential nature of the reaction also makes it essential that no part of the catalyst is nonselective.
32 For reactions in which both the desired and side products form in parallel, having a small
33 percentage of the catalyst surface showing a lower selectivity will not dramatically change the
34 overall selectivity. With a sequential reaction, the nonselective part of the catalyst can have a
35 much more dramatic effect. This has important consequences for alloy catalysts. While the
36 catalyst based on Pt₃Co₂ NCs has the necessary properties to achieve very high selectivities,
37 alloy catalysts prepared by conventional impregnation methods will not be so compositionally
38 uniform. Both Pt and Co are individually are nonselective because they are active for reactions of
39 DMF, so that any metal in the catalyst which is not in the form of an alloy will be nonselective.
40 (Note: This is indeed observed. A Pt₃Co₂ catalyst prepared by incipient wetness of the metal salts
41 showed poor control of particle size and composition (Figure S6 in SI) and a maximum
42 selectivity of less than 80% (Figure S7 of SI).)
43
44
45
46
47
48
49
50
51
52
53
54
55
56
57
58
59
60

1
2
3 In this context, it is interesting to consider the work from Schüth and co-workers¹⁷, who
4 first reported extremely high selectivities for HDO of HMF with PtCo alloys. In their case, the
5 highest selectivities were achieved when the metal particles were encapsulated in porous carbon
6 spheres. We suggest that those carbon spheres were important for achieving a high compositional
7 uniformity in the particles.
8
9

10
11 Control of the metal composition is essential in order to achieve good HDO selectivity.
12 From the HDO studies, we learned that Pt₃Co was not as selective as Pt₃Co₂. The reason for this
13 is the difference in particle surface structure. Pt₃Co does not have enough Co atoms to
14 completely cover the surface. The incomplete coverage of Co oxide leads to the presence of
15 uncovered Pt sites, and therefore causes partial non-selectivity of the Pt₃Co catalyst. While it
16 may be possible to increase the Co:Pt ratio further, a catalyst with excess Co is likely to be
17 unselective since monometallic Co catalysts are unselective.¹⁸ Catalyst stability is equally
18 important to activity and our results suggest that there is a direct correlation between stability
19 and selectivity. The most serious and rapid deactivation in our experiments was due to coking
20 which must be caused by further reaction of overhydrogenated products, such as the 2,5-
21 hexanedione. The Pt-Co alloy catalyst also seems to be more tolerant against sintering, possibly
22 as a result of the core-shell structure.
23
24

25 While the catalyst based on Pt₃Co₂ NCs exhibits excellent properties, it would obviously be
26 beneficial to find a selective catalyst that did not require a precious metal. Investigations on the
27 gas-phase reaction of furfural have shown that base-metal alloys can exhibit good selectivity for
28 the HDO reaction to methylfuran over the decarbonylation reaction to form furan.¹⁴ Also, recent
29 work by some of us demonstrated that there are many similarities between the reactions of
30 furfural and HMF, with differences due mainly to the operating conditions typically employed
31 for these reactions.⁵⁷ Therefore, it will be interesting to examine some of the compositions used
32 in the furfural reactions for HDO of HMF.
33
34

35 36 37 38 39 40 41 42 43 44 45 46 47 48 49 **CONCLUSIONS**

50 High selectivity of DMF from liquid-phase HDO of HMF with H₂ can be achieved over a
51 well-controlled Pt-Co /C catalyst. Particularly, over Pt₃Co₂ catalyst, 98% of DMF yield was
52 obtained with the optimized reaction temperature and space time. Recognizing the sequential
53 nature of the HMF HDO reaction is the key for catalyst-development strategies. Noble metals
54
55
56
57
58
59
60

1
2
3 interact strongly with the ring to promote side reactions. The fundamental principle for the
4 superior performance of Pt₃Co₂ is that the bimetallic alloy forms a monolayer oxide on the
5 surface of the metallic core that interacts weakly with the furan ring to prevent over-
6 hydrogenation and ring opening of DMF to secondary by-products while forming active sites to
7 carry out the HDO process. In this regard, composition control is crucial to cover the entire
8 surface with an oxide layer and avoid exposed metallic patches that can promote side reactions.
9 Given that HDO is commonly employed in biomass upgrade, the learnings from this study could
10 be used for the upgrade of other molecules, including bio-oil.
11
12
13
14
15
16
17
18

19 SUPPORTING INFORMATION

20 Product distributions of partially-hydrogenated and over-hydrogenated compounds,
21 particle size distributions of NCs, EXAFS fitting parameters, metal dispersions, DFT energies
22 and barriers, honeycomb structure parameters, oxide vacancy formation kinetic, TEM analysis of
23 NCs size change before and after reaction, HDO elementary reaction steps, impregnated PtCo
24 HDO performance, reaction network and energy barriers for HDO over Pt, preparation method
25 for NCs.
26
27
28
29
30
31
32

33 ACKNOWLEDGEMENTS

34 We acknowledge support from the Catalysis Center for Energy Innovation, an Energy
35 Frontier Research Center funded by the U.S. Department of Energy, Office of Science, Office of
36 Basic Energy Sciences under Award no. DE-SC0001004 and useful discussions with Prof.
37 Ayman Karim.
38
39
40
41
42
43

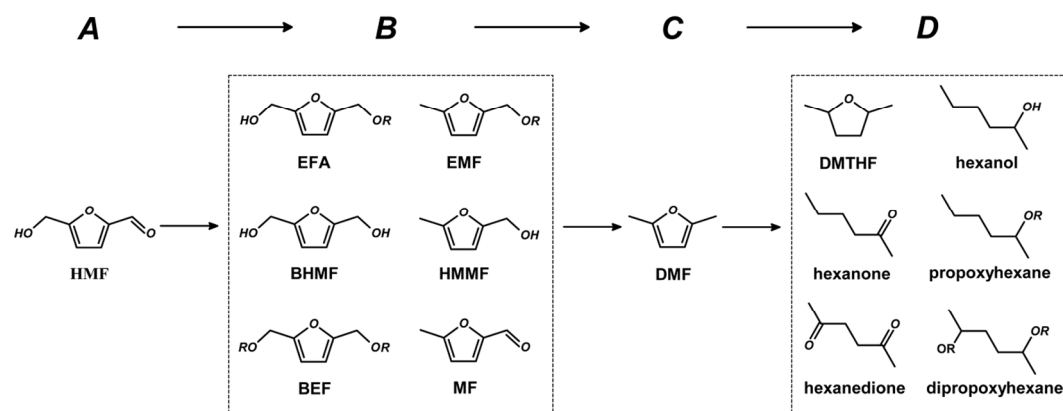
44 REFERENCES

- 45
46 (1) Román-Leshkov, Y.; Barrett, C. J.; Liu, Z. Y.; Dumesic, J. A. *Nature* **2007**, *447*, 982-985.
47 (2) Nakagawa, Y.; Tamura, M.; Tomishige, K. *ACS Catal.* **2013**, *3*, 2655-2668.
48 (3) Wang, T.; Nolte, M. W.; Shanks, B. H. *Green Chem* **2014**, *16*, 548-572.
49 (4) Dashtban, M.; Gilbert, A.; Fatehi, P. *RSC Adv* **2014**, *4*, 2037-2050.
50 (5) Torres, A. I.; Daoutidis, P.; Tsapatsis, M. *Energy Environ. Sci.* **2010**, *3*, 1560-1572.
51 (6) Chen, G.; Shen, Y.; Zhang, Q.; Yao, M.; Zheng, Z.; Liu, H. *Energy* **2013**, *54*, 333-342.
52
53
54
55
56
57
58
59
60

- 1
2
3
4
5
6
7
8
9
10
11
12
13
14
15
16
17
18
19
20
21
22
23
24
25
26
27
28
29
30
31
32
33
34
35
36
37
38
39
40
41
42
43
44
45
46
47
48
49
50
51
52
53
54
55
56
57
58
59
60
- (7) Williams, C. L.; Chang, C.-C.; Do, P.; Nikbin, N.; Caratzoulas, S.; Vlachos, D. G.; Lobo, R. F.; Fan, W.; Dauenhauer, P. J. *ACS Catal.* **2012**, *2*, 935-939.
 - (8) Chidambaram, M.; Bell, A. T. *Green Chem.* **2010**, *12*, 1253-1262.
 - (9) Thananatthanachon, T.; Rauchfuss, T. B. *Angew. Chem. Int. Ed.* **2010**, *49*, 6616-6618.
 - (10) Jae, J.; Zheng, W.; Lobo, R. F.; Vlachos, D. G. *ChemSusChem* **2013**, *6*, 1158-1162.
 - (11) Hu, L.; Tang, X.; Xu, J.; Wu, Z.; Lin, L.; Liu, S. *Ind. Eng. Chem. Res.* **2014**, *53*, 3056-3064.
 - (12) Basudeb Saha; Christine M. Bohn; Mahdi M. Abu-Omar. *ChemSusChem* **2014**, *7*, 3095-3101.
 - (13) Luo, J.; Arroyo-Ramírez, L.; Gorte, R. J.; Tzoulaki, D.; Vlachos, D. G. *AIChE J.* **2015**, *61*, 590-597.
 - (14) Sitthisa, S.; An, W.; Resasco, D. E. *J. Catal.* **2011**, *284*, 90-101.
 - (15) Myint, M.; Yan, Y.; Chen, J. G. *J. Phys. Chem. C* **2014**, *118*, 11340-11349.
 - (16) Lee, J.; Kim, Y. T.; Huber, G. W. *Green Chem.* **2014**, *16*, 708-718.
 - (17) Wang, G.-H.; Hilgert, J.; Richter, F. H.; Wang, F.; Bongard, H.-J.; Spliethoff, B.; Weidenthaler, C.; Schüth, F. *Nat. Mater.* **2014**, *13*, 293-300.
 - (18) Luo, J.; Arroyo-Ramírez, L.; Wei, J.; Yun, H.; Murray, C. B.; Gorte, R. J. *Appl. Catal. Gen.* **2015**, *508*, 86-93.
 - (19) Shevchenko, E. V.; Talapin, D. V.; Rogach, A. L.; Kornowski, A.; Haase, M.; Weller, H. *J. Am. Chem. Soc.* **2002**, *124*, 11480-11485.
 - (20) Cargnello, M.; Doan-Nguyen, V. V. T.; Gordon, T. R.; Diaz, R. E.; Stach, E. a; Gorte, R. J.; Fornasiero, P.; Murray, C. B. *Science* **2013**, *341*, 771-773.
 - (21) Gordon, T. R.; Cargnello, M.; Paik, T.; Mangolini, F.; Weber, R. T.; Fornasiero, P.; Murray, C. B. *J. Am. Chem. Soc.* **2012**, *134*, 6751-6761.
 - (22) Huang, X.; Cao, L.; Chen, Y.; Zhu, E.; Lin, Z.; Li, M.; Yan, A.; Zettl, A.; Wang, Y. M.; Duan, X.; Mueller, T. *Science* **2015**, *348*, 1230-1234.
 - (23) Mironenko, A. V.; Vlachos, D. G. *Under Review*.
 - (24) Fievet, F.; Lagier, J.; Blin, B.; Beaudoin, B.; Figlarz, M. *Solid State Ion.* **1989**, 32-33, 198-215.
 - (25) Yu, Y.; Yang, W.; Sun, X.; Zhu, W.; Li, X. Z.; Sellmyer, D. J.; Sun, S. *Nano Lett.* **2014**, *14*, 2778-2782.

- 1
2
3
4
5
6
7
8
9
10
11
12
13
14
15
16
17
18
19
20
21
22
23
24
25
26
27
28
29
30
31
32
33
34
35
36
37
38
39
40
41
42
43
44
45
46
47
48
49
50
51
52
53
54
55
56
57
58
59
60
- (26) Cargnello, M.; Chen, C.; Diroll, B. T.; Doan-Nguyen, V. V. T.; Gorte, R. J.; Murray, C. B. *J. Am. Chem. Soc.* **2015**, *137*, 6906-6911.
- (27) Wang, D.; Xin, H. L.; Hovden, R.; Wang, H.; Yu, Y.; Muller, D. a.; DiSalvo, F. J.; Abruña, H. D. *Nat. Mater.* **2012**, *12*, 81-87.
- (28) Tengco, J. M. M.; Lugo-José, Y. K.; Monnier, J. R.; Regalbuto, J. R. *Catal. Today* **2015**, *246*, 9-14.
- (29) Scholten, J. J. F.; Pijpers, A. P.; Hustings, A. M. L. *Catal. Rev. Sci. Eng.* **1985**, *27*, 151-206.
- (30) Kresse, G.; Hafner, J. *Phys. Rev. B* **1993**, *47*, 558-561.
- (31) Kresse, G.; Furthmüller, J. *Comput. Mater. Sci.* **1996**, *6*, 15-50.
- (32) Kresse, G.; Furthmüller, J. *Phys. Rev. B* **1996**, *54*, 11169-11186.
- (33) Monkhorst, H. J.; Pack, J. D. *Phys. Rev. B* **1976**, *13*, 5188-5192.
- (34) Perdew, J. P.; Burke, K.; Ernzerhof, M. *Phys. Rev. Lett.* **1996**, *77*, 3865-3868.
- (35) Grimme, S.; Antony, J.; Ehrlich, S.; Krieg, H. *J. Chem. Phys.* **2010**, *132*, 154104-154104.
- (36) Henkelman, G.; Jonsson, H. *J. Chem. Phys.* **2000**, *113*, 9978-9978.
- (37) Henkelman, G.; Uberuaga, B. P.; Jónsson, H. *J. Chem. Phys.* **2000**, *113*, 9901-9901.
- (38) Sheppard, D.; Terrell, R.; Henkelman, G. *J. Chem. Phys.* **2008**, *128*, 134106-134106.
- (39) Sheppard, D.; Henkelman, G. *J. Comput. Chem.* **2011**, *32*, 1769-1771.
- (40) Ng, Y. H.; Ikeda, S.; Harada, T.; Sakata, T.; Mori, H.; Takaoka, A.; Matsumura, M. *Langmuir* **2008**, *24*, 6307-6312.
- (41) Lonergan, W. W.; Vlachos, D. G.; Chen, J. G. *J. Catal.* **2010**, *271*, 239-250.
- (42) Menning, C. A.; Chen, J. G. *J. Chem. Phys.* **2008**, *128*, 164703-164703.
- (43) De Santis, M.; Buchsbaum, A.; Varga, P.; Schmid, M. *Phys. Rev. B* **2011**, *84*, 125430-125430.
- (44) Blaylock, D. W.; Zhu, Y.-A.; Green, W. H. *Top. Catal.* **2011**, *54*, 828-844.
- (45) Zhu, Z.; Tao, F.; Zheng, F.; Chang, R.; Li, Y.; Heinke, L.; Liu, Z.; Salmeron, M.; Somorjai, G. A. *Nano Lett.* **2012**, *12*, 1491-1497.
- (46) Knudsen, J.; Merte, L. R.; Grabow, L. C.; Eichhorn, F. M.; Porsgaard, S.; Zeuthen, H.; Vang, R. T.; Lægsgaard, E.; Mavrikakis, M.; Besenbacher, F. *Surf. Sci.* **2010**, *604*, 11-20.
- (47) Tuokko, S.; Pihko, P. M.; Honkala, K. *Angew. Chem. Int. Ed.* **2016**, *55*, 1670-1674.
- (48) Loffreda, D.; Delbecq, F.; Vigné, F.; Sautet, P. *J. Am. Chem. Soc.* **2006**, *128*, 1316-1323.

- 1
2
3
4 (49) Caratzoulas, S.; Vlachos, D. G. *Carbohydr. Res.* **2011**, *346*, 664-672.
5
6 (50) Mironenko, A. V.; Gilkey, M. J.; Panagiotopoulou, P.; Facas, G.; Vlachos, D. G.; Xu, B. *J.*
7 *Phys. Chem. C* **2015**, *119*, 6075-6085.
8
9 (51) Wang, S.; Vorotnikov, V.; Vlachos, D. G. *Acs Catal.* **2014**, *5*, 104-112.
10 (52) Vorotnikov, V.; Mpourmpakis, G.; Vlachos, D. G. *Acs Catal.* **2012**, *2*, 2496-2504.
11 (53) Wang, S.; Vorotnikov, V.; Vlachos, D. G. *Green Chem.* **2014**, *16*, 736-747.
12 (54) Pang, S. H.; Schoenbaum, C. A.; Schwartz, D. K.; Medlin, J. W. *Nat. Commun.* **2013**, *4*,
13 *1-6*.
14 (55) Pang, S. H.; Schoenbaum, C. A.; Schwartz, D. K.; Medlin, J. W. *Acs Catal.* **2014**, *4*, 3123-
15 3131.
16
17 (56) Schoenbaum, C. A.; Schwartz, D. K.; Medlin, J. W. *Acc. Chem. Res.* **2014**, *47*, 1438-1445.
18 (57) Luo, J.; Monai, M.; Yun, H.; Arroyo-Ramírez, L.; Wang, C.; Murray, C. B.; Fornasiero, P.;
19 Gorte, R. J. *Catal. Lett.* **2016**, *146*, 711-717.
20
21
22
23
24
25
26
27
28
29
30
31
32
33
34
35
36
37
38
39
40
41
42
43
44
45
46
47
48
49
50
51
52
53
54
55
56
57
58
59
60



Scheme 1. Reaction network for HMF hydrodeoxygenation using alcohols as solvent.

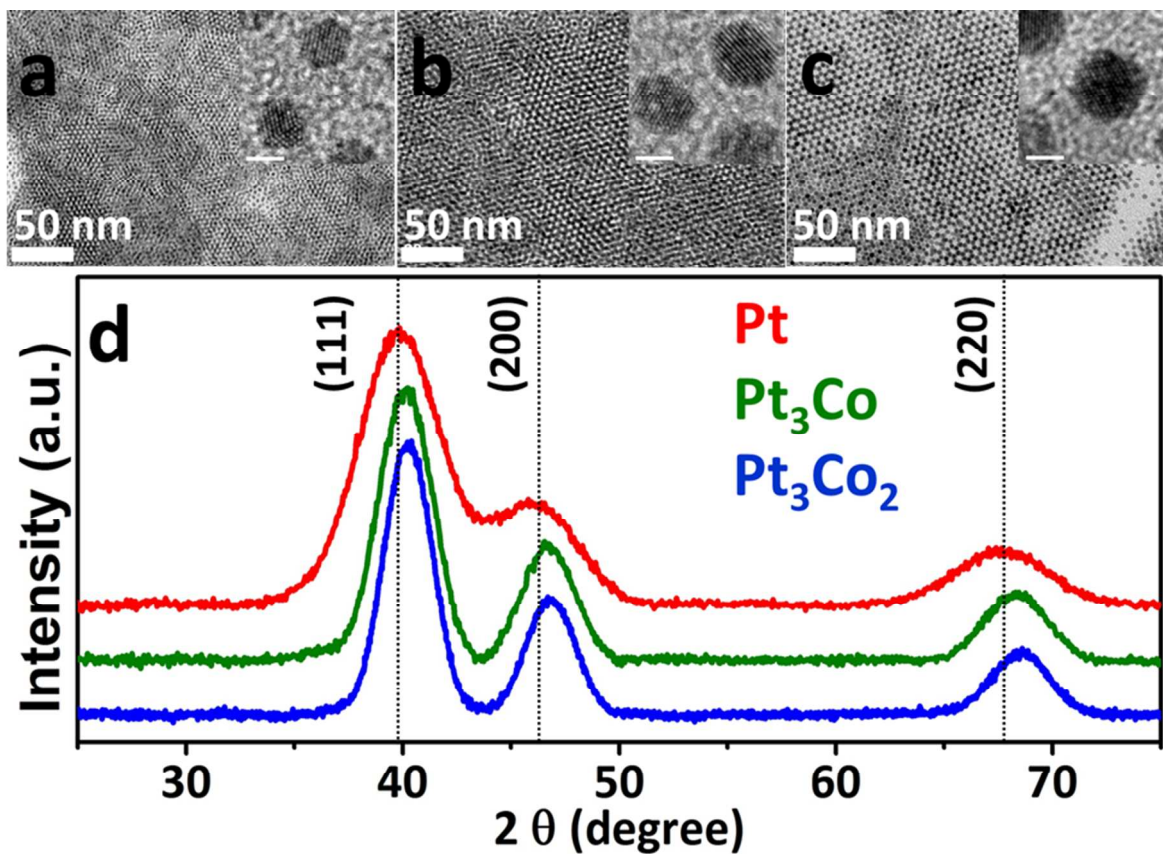


Figure 1. The TEM images of a) Pt NCs, b) Pt₃Co NCs, and c) Pt₃Co₂ NCs, after removing the solvent. d) Wide angle x-ray scattering data of Pt (red), Pt₃Co (green), and Pt₃Co₂ (blue). The scale bars in the insets represent 2 nm.

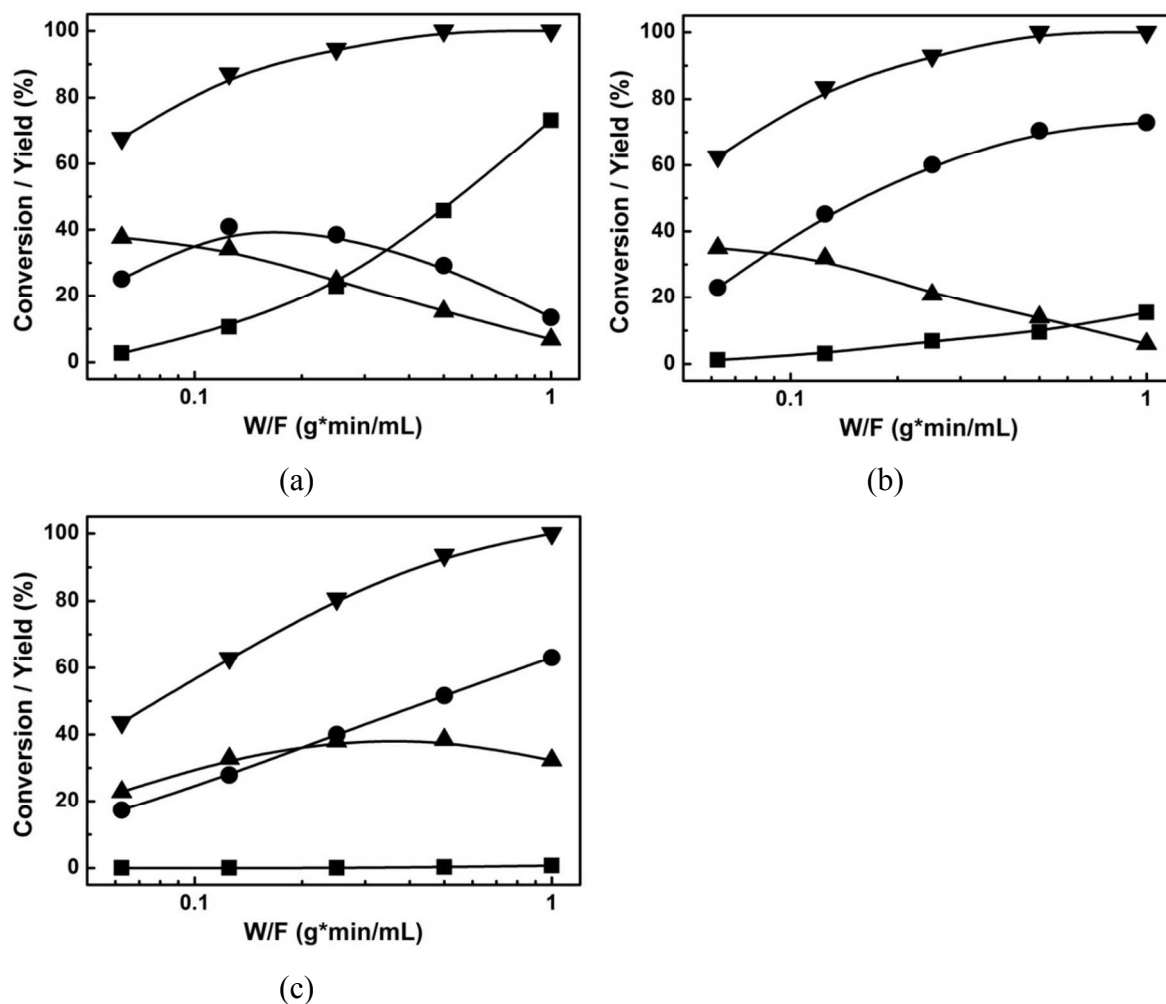


Figure 2. Conversion and product distribution for the HDO reaction of HMF over (a) 10-wt% Pt/C, (b) 10-wt% Pt₃Co/C, (c) 10-wt% Pt₃Co₂/C, as a function of reactor space time. Reaction conditions: 33 bar and 120 °C. (▼) HMF conversion, (▲) product group B, (●) DMF, (■) product group D

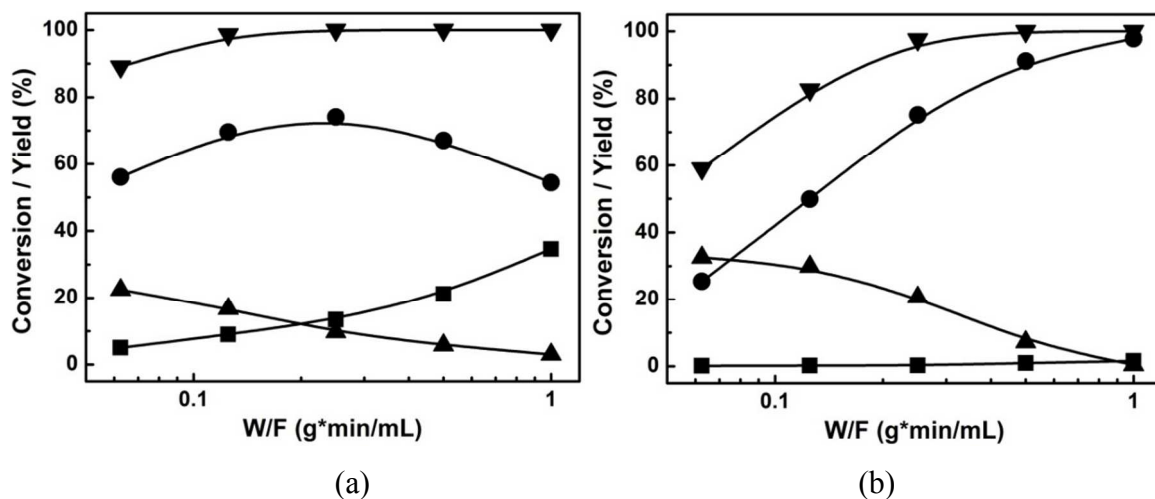


Figure 3. Conversion and product distribution for the HDO reaction of HMF over (a) 10-wt% Pt₃Co/C, (b) 10-wt% Pt₃Co₂/C, as a function of reactor space time. Reaction conditions: 33 bar and 160 °C. (▼) HMF conversion, (▲) product group B, (●) DMF, (■) product group D

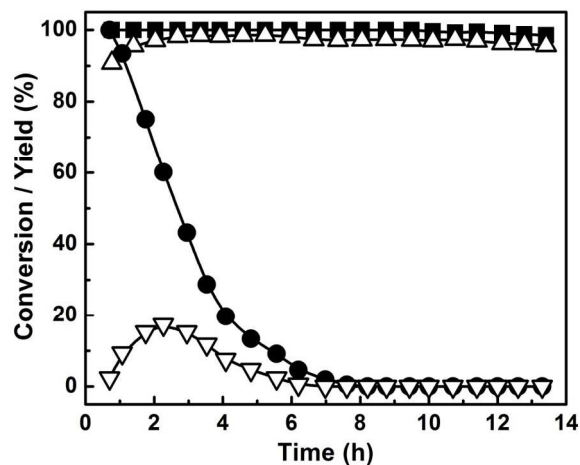


Figure 4. Time on stream measurements for HMF hydrodeoxygenation. Reaction conditions: 33 bar, 160 °C, W/F 1.0 g·min/mL. (■) HMF conversion over 10-wt% Pt₃Co₂/C, (△) DMF yield over 10-wt% Pt₃Co₂/C, (●) HMF conversion over 10-wt% Pt/C, (▽) DMF yield over 10-wt% Pt/C

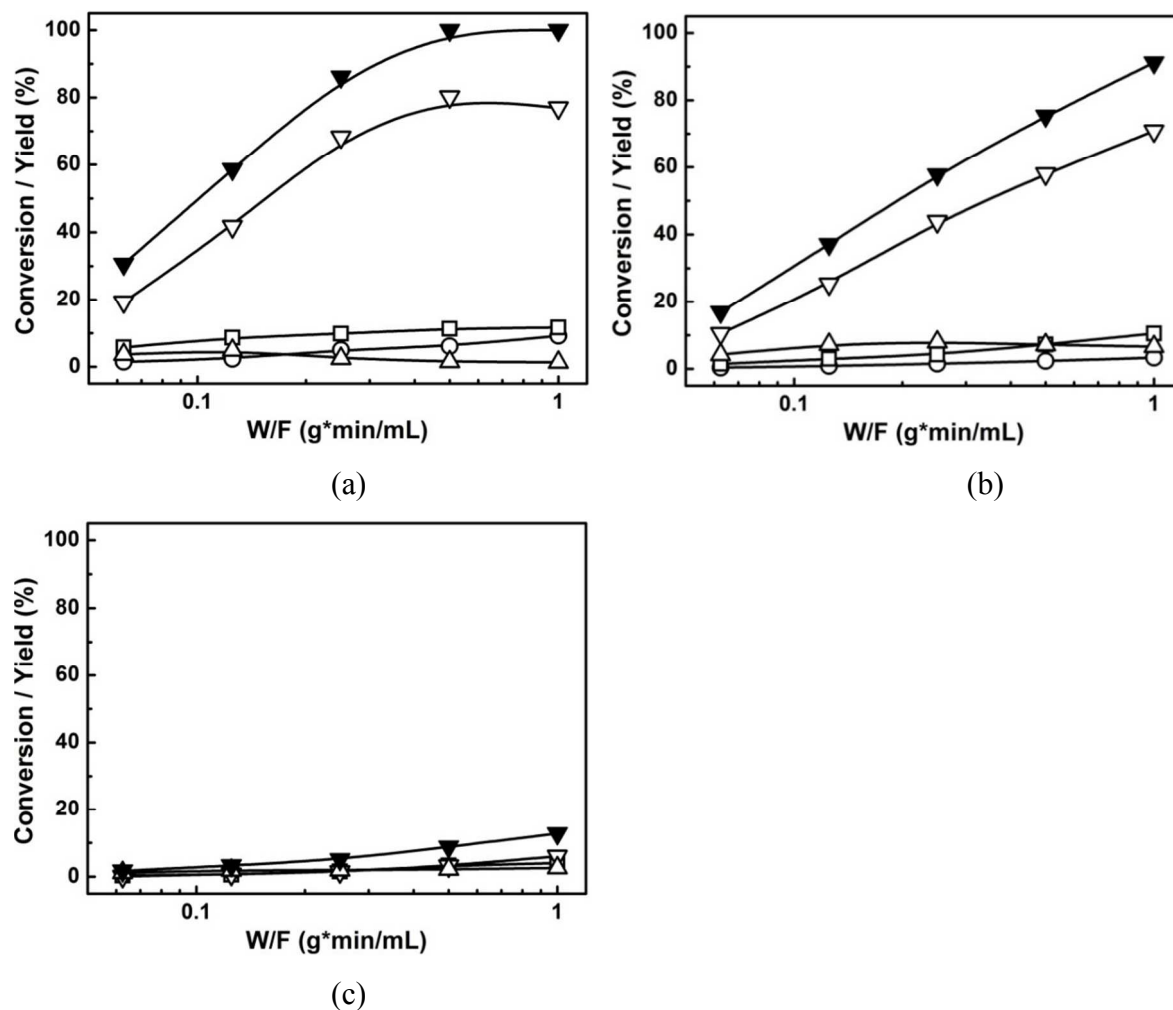


Figure 5. Conversion and product distribution for the reaction of DMF as a function of space time at 33 bar: (a) 10-wt% Pt/C at 120 °C; (b) 10-wt% Pt₃Co/C at 160 °C, (c) 10-wt% Pt₃Co₂/C at 160 °C. (▼) DMF conversion, (□) DMTHF, (▽) 2-hexanone, 2-hexanol and 2-propoxyhexane, (△) 2,5-hexandione, 2,5-dipropoxyhexane, (○) hexane

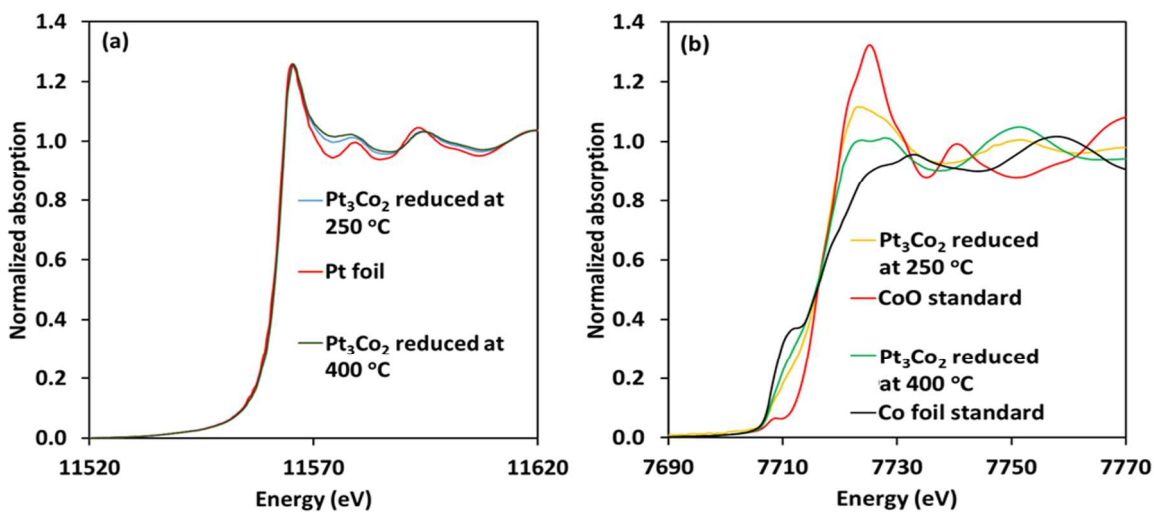


Figure 6. (a) Pt L3 edge XANES. Pt foil (red), Pt₃Co₂ reduced at 250 °C (blue) and Pt₃Co₂ reduced at 400 °C (black). (b) Co K edge XANES. Co foil standard (black), CoO standard (red), Pt₃Co₂ reduced at 250 °C (yellow) and Pt₃Co₂ reduced at 400 °C (green).

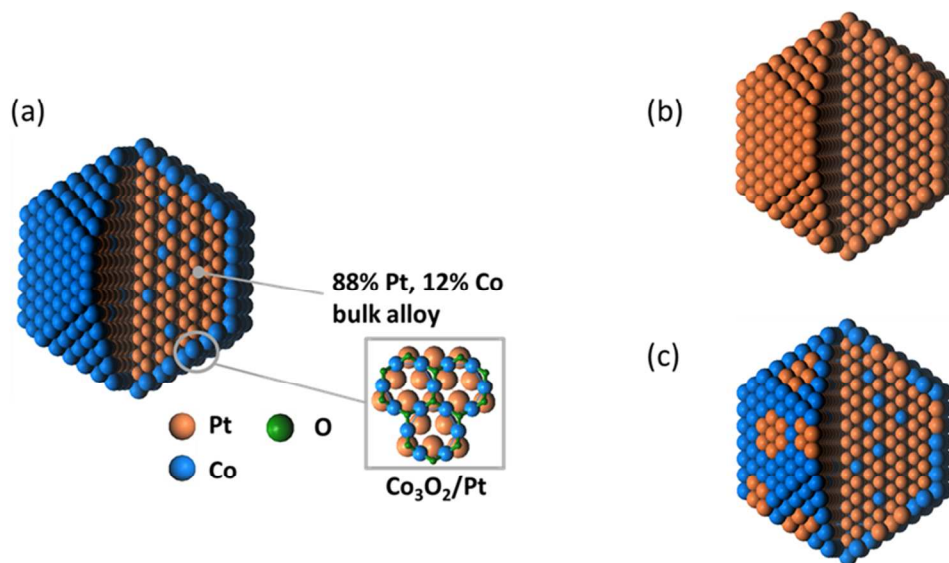


Figure 7. (a) Pt₃Co₂ nanocrystal model involving an alloy core (88% Pt, 12% Co based on XRD) covered with a Co₃O₂ surface oxide monolayer with a honeycomb structure; (b) and (c) correspond to Pt and Pt₃Co NC models.

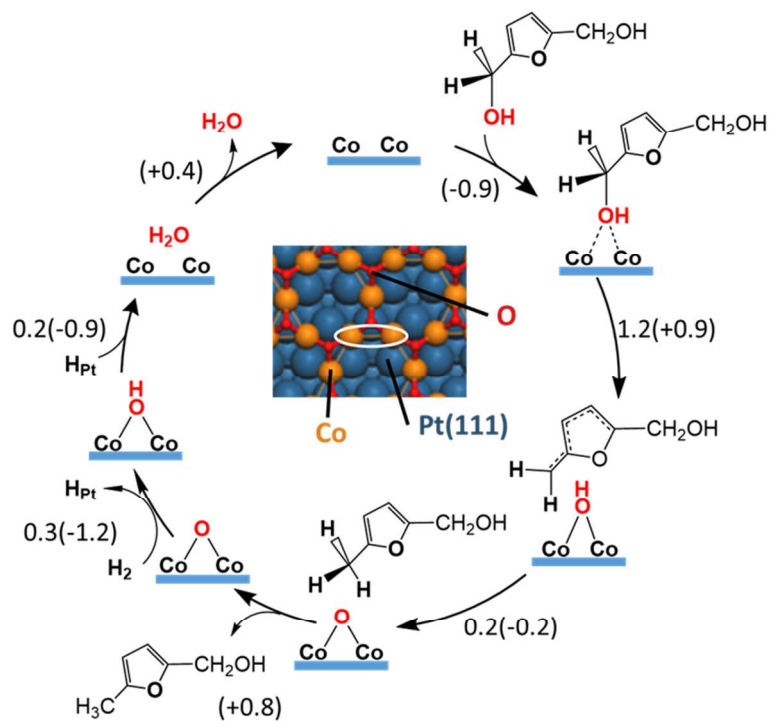


Figure 8. Reaction mechanism of BHMF hydrodeoxygenation to HMMF on the $\text{Co}_3\text{O}_2/\text{Pt}(111)$ surface. DFT reaction barriers (energies) are given in eV. The inset depicts a portion of a $\text{Co}_3\text{O}_2/\text{Pt}(111)$ surface. Two Co atoms participating in C-O bond activation are encircled with a white ellipsoid.

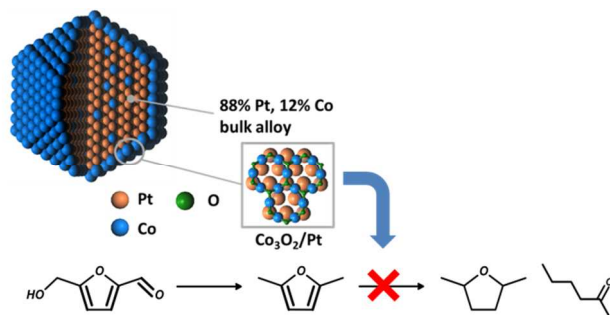


Table of Contents Graphic